ARCHIVES OF ELECTRICAL ENGINEERING VOL. X(Y), pp. 1-23 (2026)

This paper has been accepted for publication in the AEE journal. This is the version, which has not been fully edited and content may change prior to final publication.
Citation information: DOI 10.24425/aee.2026.158261

Bringing automation to electromagnetic by robotic scanning of magnetic field in electric drives

HUBERT MILANOWSKI, ADAM KRZYSZTOF PIŁAT*

Faculty of Electrical Engineering, Automatics, Computer Science and Biomedical Engineering
Department of Automatic Control and Robotics, AGH University of Krakow
al. A. Mickiewicza 30, 30-059 Krakow, Poland
*e-mail:{milan/*ap}@agh.edu.pl*

Abstract: Accurate magnetic field measurement is vital for analysing and optimizing electric machines such as permanent magnet synchronous motors. Existing methods struggle with complex geometries, enclosed structures, and multi-axis field variations. We propose a robotic arm-based system for automated, high-resolution scanning of all three magnetic field components across the full motor geometry, including stator and rotor. The system enables precise sensor positioning on curved surfaces for reliable data acquisition where traditional setups fail. Comprehensive spatial analysis, including harmonic decomposition, reveals hidden field patterns that support improved diagnostics and motor design. This flexible, scalable approach advances both experimental research and industrial evaluation of electric machines.

Key words: electric drives, industrial automation, magnetic field analysis, motor diagnostics, robotic scanning

1. Introduction

In an era of rapid electrification across multiple industries, the global electric motor market is projected to exceed USD 250 billion by 2032. Growing demand from industrial automation, electric vehicles, and renewable energy systems raises a critical challenge: further improving motor efficiency. While advances in materials and optimised design methodologies have significantly enhanced performance, one fundamental yet often underappreciated factor remains pivotal - the magnetic field governing motor control.

Accurate magnetic field measurement is essential for motor design, control, and fault diagnosis. During the design stage, it enables the optimisation of stator and rotor geometries [1], winding configurations [2], and material selection, thereby improving efficiency and reducing losses. In permanent magnet synchronous motors (PMSMs), refined magnetic flux paths reduce cogging torque and promote smoother operation [3]. In control strategies, real-time or pre-measured magnetic field data supports sensorless position estimation, force generation, and torque optimisation [4, 5]. In PMSMs, enhanced magnetic flux information obtained from Hall-

This paper has been accepted for publication in the AEE journal. This is the version, which has not been fully edited and content may change prior to final publication.
Citation information: DOI 10.24425/aee.2026.158261

effect sensors [6] and flux-linkage-based estimation methods [7] improves drive accuracy, which is particularly important in applications such as industrial robotic manipulators requiring high-precision motion and repeatability. Deviations in magnetic field distribution can also indicate faults such as demagnetisation, mechanical misalignment, or insulation degradation [8]. More broadly, detailed knowledge of magnetic field distributions underpins advanced modelling, state estimation, and control techniques across a wide range of electrical machine topologies [9–11].

Measuring magnetic fields remains challenging due to their intangible nature and sensitivity to environmental conditions. Consequently, numerous techniques have been developed, each tailored to specific accuracy and application requirements. Hall-effect sensors are widely used in industrial settings owing to their compact size, low cost, and ease of integration, for example, in large-area quality-control scanning [12]. Fluxgate magnetometers provide higher sensitivity for low-field environments [13], while optically pumped magnetometers offer ultra-sensitive field detection for high-precision applications [14]. Despite their advantages, all these approaches face a common limitation: achieving accurate, repeatable, and efficient measurements in complex and constrained environments.

To address this limitation, several state-of-the-art magnetic field measurement systems have been proposed. Large-area magnetic field cameras enable high-speed, real-time field mapping for inline magnet inspection [15] but are restricted to flat or open geometries due to fixed sensor configurations. More advanced three-dimensional (3D) and six-dimensional (6D) magnetic field cameras provide vector field measurements [16, 17], offering a more comprehensive representation of magnetic structures; however, they remain constrained by slow scanning speeds and rigid mechanical setups.

Magnetic flux leakage (MFL) inspection techniques [18] are widely used for defect detection in ferromagnetic structures, employing Hall-effect or magneto resistive sensors to identify anomalies in applications such as pipeline integrity monitoring. Nevertheless, MFL lacks the spatial resolution and adaptability required for complex electrical machine components. Similarly, scanning Hall probe microscopes achieve exceptional microscale resolution [19] but are limited by slow scanning speeds and sensitivity to environmental disturbances, confining their use largely to laboratory environments.

Cartesian XYZ positioning systems have also been employed for magnetic field scanning, providing basic three-dimensional coverage via linear motion stages. Examples include low-cost modular systems for mapping permanent magnets [20] and configurations used to investigate electromagnet-generated fields [21]. Although such systems enable volumetric measurements, their linear-axis constraints limit their suitability for complex, enclosed, or irregular electrical machine geometries.

Robotic automation has transformed numerous industrial and research fields by improving precision, repeatability, and efficiency. Robotic manipulators are widely used for quality-control inspection [22], high-throughput biomedical experimentation [23], and electric motor manufacturing tasks such as coil winding and automated assembly [24]. Despite these advances, the application of robotics to electric motor testing and commissioning - particularly for magnetic field measurement - remains limited.

This paper has been accepted for publication in the AEE journal. This is the version, which has not been fully edited and content may change prior to final publication.
Citation information: DOI 10.24425/aee.2026.158261

To address this gap, this paper presents an automated robotic-arm-based magnetic field scanning system equipped with a high-precision sensor. The proposed system systematically scans electric machine surfaces to acquire high-resolution magnetic field data with improved accuracy, repeatability, and adaptability. Unlike conventional approaches, it ensures precise sensor positioning and accommodates a wide range of machine geometries, thereby enhancing experimental efficiency and data richness. An earlier stage of this work was reported in [25], which forms the foundation for the developments presented here.

2. Robotic magnetic field scan system: components and configuration

2.1. System architecture

The system architecture is designed for high-precision magnetic field mapping during radial scanning of individual electric motor components. Based on preliminary magnetic field identification studies [21], a dedicated measurement probe was developed, as shown in Fig. 1. The probe integrates a custom magnetic sensing unit comprising three coaxially aligned Hall-effect sensors (Honeywell SS49E) with a measurement range of ±100 mT.

Mounted on a robotic arm, the probe enables accurate positioning while maintaining the required sensor distance and orientation. Figure 2 illustrates the sensor reference frames relative to the tool centre point (TCP) of the robotic arm. As the sensors are spatially offset from the TCP, their measurements correspond to distinct locations. During post-processing, these offsets are combined with the recorded TCP positions to map the magnetic flux density components to their true spatial coordinates, ensuring an accurate and high-resolution magnetic field representation. The exact displacements of the Hall-effect sensors relative to the TCP are summarised in Table 1.

Measurement data are acquired in real time using data acquisition (DAQ) cards installed in a standard PC. The system employs two types of analogue-to-digital converter (ADC) cards: a Humusoft card with simultaneous sampling and a National Instruments (NI) card with multiplexed sampling. The Humusoft card acquires all sensor signals concurrently, thereby eliminating inter-channel timing delays. Although the NI card relies on multiplexed ADCs, its high sampling rate and short switching times enable accurate reconstruction of magnetic field dynamics. With a sampling frequency of 10 kHz, the system provides high temporal resolution, allowing the complete magnetic field state to be captured within a single measurement interval and ensuring synchronised data acquisition.

The measurement process is fully automated using custom software developed in MATLAB/Simulink, which manages system modules and provides an interface for pre-measurement configuration, real-time monitoring, and data visualisation. The robotic arm operates under a dedicated motion control program executed on its internal controller, while the scan trajectory is dynamically transmitted from the PC via the Remote Motion Interface (RMI), ensuring precise synchronisation between robotic motion and data acquisition.

This paper has been accepted for publication in the AEE journal. This is the version, which has not been fully edited and content may change prior to final publication.
Citation information: DOI 10.24425/aee.2026.158261

Controlled magnetic field excitation during testing is achieved by generating a 1 kHz voltage reference signal for the hardware current drivers supplying the stator coils. Six independent current drivers regulate the excitation of each stator pole coil, ensuring stable and repeatable operation. Each driver is based on an LMD 18245 full-bridge power amplifier employing a fixed off-time chopper technique with internal current feedback to regulate current flow throughthe stator windings.

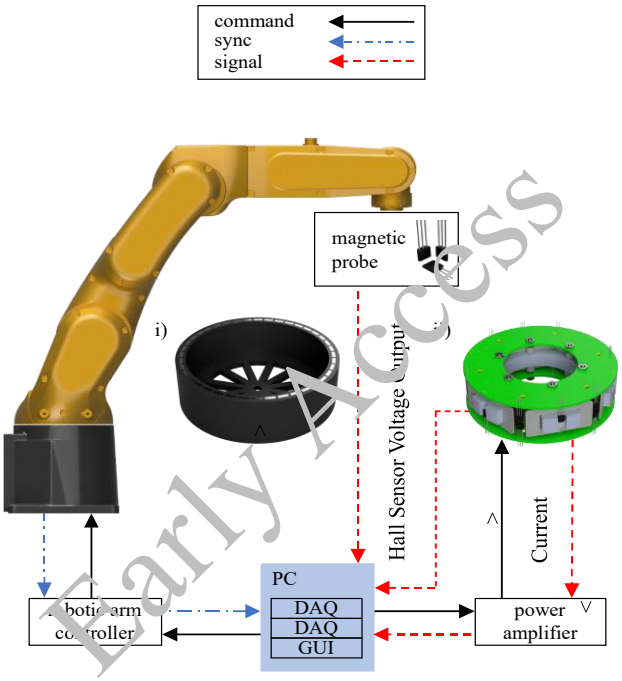

Fig. 1. Schematic of a robotic magnetic field scan system: case i) concerns rotor scan, whereas ii) stator scan

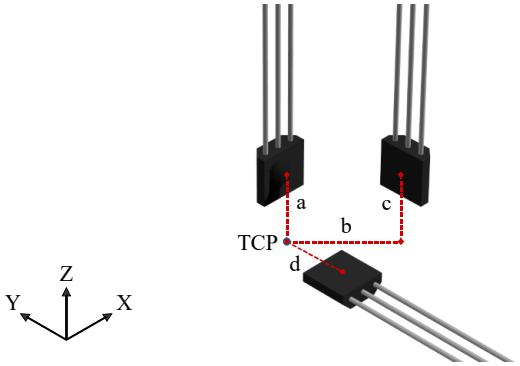

Fig. 2. Hall sensor positions relative to the tool centre point (TCP)

This paper has been accepted for publication in the AEE journal. This is the version, which has not been fully edited and content may change prior to final publication.
Citation information: DOI 10.24425/aee.2026.158261

Table1. Translational displacement of sensors relative to TCP

Displacement	Direction	Distance (mm)
a	*z*	3
b	*x*	3.25
c	*z*	3
d	*y*	3.25

2.2. System operation

To ensure measurement accuracy, an initial calibration procedure is performed prior to scanning, including calibration of the tool centre point (TCP) to account for the geometry of the measurement probe during radial scanning. The necessary offsets are determined using CAD models of the scanned components, ensuring accurate positioning.

A second calibration step establishes the origin of the coordinate system for the scanned region, typically the geometric centre of the rotor or stator. Where higher precision is required, laser-based measurement systems may determine exact spatial relationships. Without additional instrumentation, rotor alignment is achieved using adjustable mounts and an iterative procedure. Slotted mounting holes allow controlled manual adjustments, and repeated rotation with measurement validation progressively refines alignment to minimise offsets and ensure stable positioning.

After calibration, the scan area is defined, with the trajectory derived from the geometry of the object. Once scan boundaries are set, a grid is generated specifying TCP position and orientation throughout the measurement. These data are transformed from the sensor coordinate frame into the robot base frame for spatial alignment, and orientation data are converted to the robot wrist frame to maintain proper probe orientation.

Prior to execution, the scan grid is checked for reachability and collision avoidance. Depending on the scenario, different scanning strategies may be applied. In radial scanning of rotor or stator components, the probe moves continuously at a controlled velocity along the scanning plane to ensure uniform data acquisition.

A trigger signal synchronises magnetic field data acquisition with robotic motion. Scan paths may be generated offline using predefined patterns, CAD-based models, or adaptive trajectories with real-time sensor feedback. Once finalised, the scan grid is transmitted to the robot controller via TCP/IP using the Remote Motion Interface (RMI), enabling reliable execution of the measurement process.

2.3. Measurement uncertainty analysis

The total uncertainty of the measurement system described above is influenced by multiple independent error sources, including Hall-effect sensor inaccuracies, analogue-to-digital converter (ADC) quantisation, and positioning errors. The combined uncertainty is estimated

This paper has been accepted for publication in the AEE journal. This is the version, which has not been fully edited and content may change prior to final publication.
Citation information: DOI 10.24425/aee.2026.158261

using the root-sum-of-squares (RSS) method, with a detailed derivation provided in the supplementary material [26].

Based on the analysis, the measurement uncertainty ranges from ±1.95 mT in the best-case scenario to ±5.26 mT in the worst-case scenario, with a typical uncertainty of ±4.21 mT.

The first category of errors comprises intrinsic sensor-related inaccuracies. Hall-effect sensors typically exhibit a precision of ±2% of the measured value, an effect becomes more pronounced at low magnetic field strengths. Additional uncertainty arises from ADC quantisation; however, its influence is reduced using a 14-bit resolution. These factors contribute to a systematic measurement uncertainty that can be analytically quantified.

The second category includes mechanical misalignment, probe mounting tolerances, and the repeatability of robotic positioning. In the case of the Fanuc LR Mate 200iD, the specified positioning repeatability is 0.01 mm, which may introduce small deviations in measurement accuracy. Furthermore, the accuracy of the probe is affected by its manufacturing method. In this study, the probe is produced using 3D printing with a dimensional precision of 0.1 mm, introducing an additional source of variability.

Unlike sensor-related errors, these mechanical factors influence measurement accuracy in a manner that depends on the spatial distribution of the magnetic field. Identical displacement errors may therefore result in different flux density deviations, depending on the local magnetic field gradient of the machine under test. Consequently, the impact of positioning errors cannot be expressed as a fixed value and must be evaluated individually for each scanned specimen.

3. Experimental results

3.1. Design under test

This study investigates a prototype drive featuring an external rotor. The concept is based on a previously developed drive with an elliptical rotor, for which numerical analyses confirmed feasibility [27]. In addition, growing interest in humanoid robotics [28], together with a detailed assessment of propulsion requirements, motivated the development of a thin-walled drive. To support both research directions, a stator with external poles was designed, enabling flexible experimentation with different rotor configurations, as well as studies in identification, modelling, and control. The stator has a thickness of 10 mm and an outer diameter of 95 mm. It incorporates six independently controlled coils, each with a resistance of 1.21 Ω and an inductance of 592 μH (measured at 10 kHz). The rotor was designed with eight magnetic poles, each consisting of five N38-grade magnetic bars arranged along an outer diameter of 106 mm. Figure 3 shows the manufactured rotor and stator assemblies.

This paper has been accepted for publication in the AEE journal. This is the version, which has not been fully edited and content may change prior to final publication.
Citation information: DOI 10.24425/aee.2026.158261

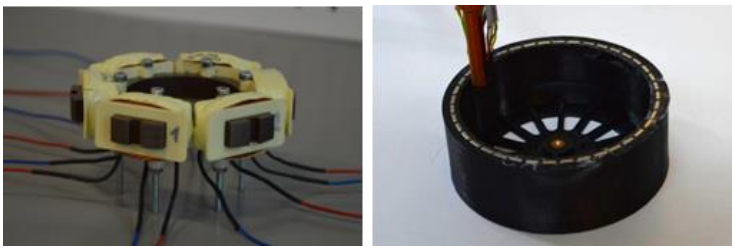

Fig. 3. Components of the designed drive

3.2. Rotor radial scan

Graphs illustrate the spatial distribution of the three magnetic field components in the rotor system: the normal (B_n), tangential ($B_{\tan}$), and binormal (B_b) components. The definition of these components within the probe reference frame is provided in Fig. 4.

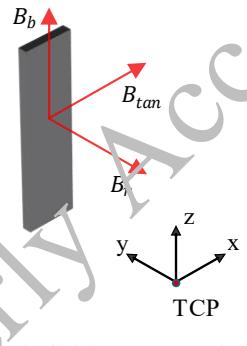

Fig. 4. Representation of magnetic field components in the probe's reference frame

Figures 5–7 show the spatial distributions of the magnetic field components corresponding to (B_n), ($B_{\tan}$), and (B_b) respectively. Each component is presented as a function of the rotational angle (θ) and either the radial position (r) or the axial height (h), with the figures corresponding to a one-eighth scan of the rotor. In each set, the left plots show the magnetic field distribution in the radial plane at the central axial position, while the right plots depict the axial variation at the maximum scanned radius, corresponding to the closest proximity to the magnet surface. A red-to-blue colour gradient indicates field intensity, with red representing positive values and blue negative values.

The normal component (B_n) shows a clear dependence on both θ and r, with its magnitude increasing towards larger radial positions. In the radial plane, the field distribution exhibits an exponential trend. Along the axial direction, a pronounced decay is observed, with the field strength peaking at the central height of the rotor and decreasing towards the outer boundaries. This behaviour is primarily governed by geometric boundary conditions and the inherent structure of the rotor magnetisation profile. Comparable field characteristics were reported by

This paper has been accepted for publication in the AEE journal. This is the version, which has not been fully edited and content may change prior to final publication.
Citation information: DOI 10.24425/aee.2026.158261

Cheng *et al*. (2015), who analysed the influence of rotor geometry on magnetic flux distribution in permanent magnet synchronous motors [29].

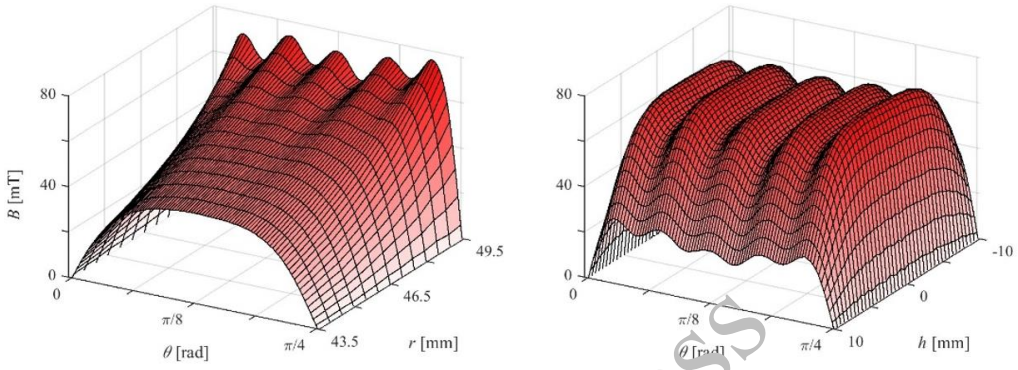

(a) (b)

Fig. 5. Rotor magnetic flux density distribution of the normal component (B_n) as a function of angular and (a) radial position, (b) axial height

The tangential component ($B_{\tan}$) exhibits more complex behaviour. It transitions smoothly between positive and negative values, forming a distinct dipolar structure. Notably, $B_{\tan}$ maintains significant magnitude in both the radial and axial planes, indicating a key role in governing the dynamic characteristics of the rotor magnetic field. This behaviour is consistent with studies on interior permanent magnet brushless DC motors (IPM BLDCMs), which show that variations in slot opening and air-gap length significantly influence magnetic flux behaviour and tangential field distribution [30].

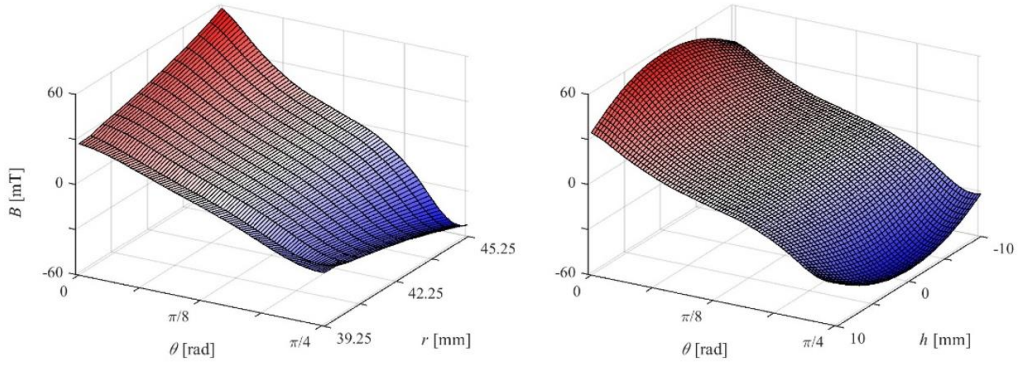

(a) (b)

Fig. 6. Rotor magnetic flux density distribution of the tangential component ($B_{\tan}$) as a function of angular and (a) radial position, (b) axial height

This paper has been accepted for publication in the AEE journal. This is the version, which has not been fully edited and content may change prior to final publication.
Citation information: DOI 10.24425/aee.2026.158261

In contrast, the binormal component, (B_b), exhibits a lower overall magnitude than (B_n) and ($B_{\tan}$), confirming its secondary contribution to magnetic field structure. The dominant normal component (B_n) governs the structural alignment of the field and may therefore influence radial forces, while the tangential component ($B_{\tan}$) determines the rotational characteristics. The binormal component (B_b) accounts for finer perturbations that may affect localised phenomena in practical applications.

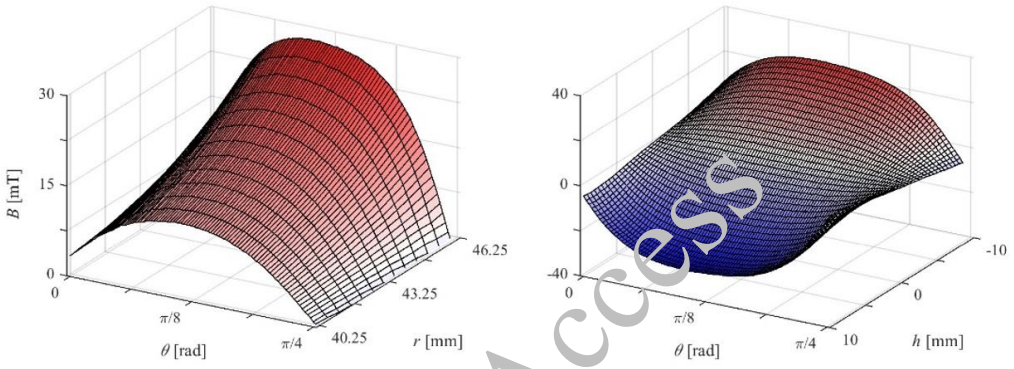

(a) (b)

Fig. 7. Rotor magnetic flux density distribution of the binormal component (B_b) as a function of angular and (a) radial position, (b) axial height

Figure 8 presents isoline plots of the normal (B_n) and tangential ($B_{\tan}$) magnetic field components at the central axial height, providing a detailed view of the field distribution across the rotor cross-section. The contour lines represent regions of equal magnetic field strength, offering an intuitive visualization of field variations.

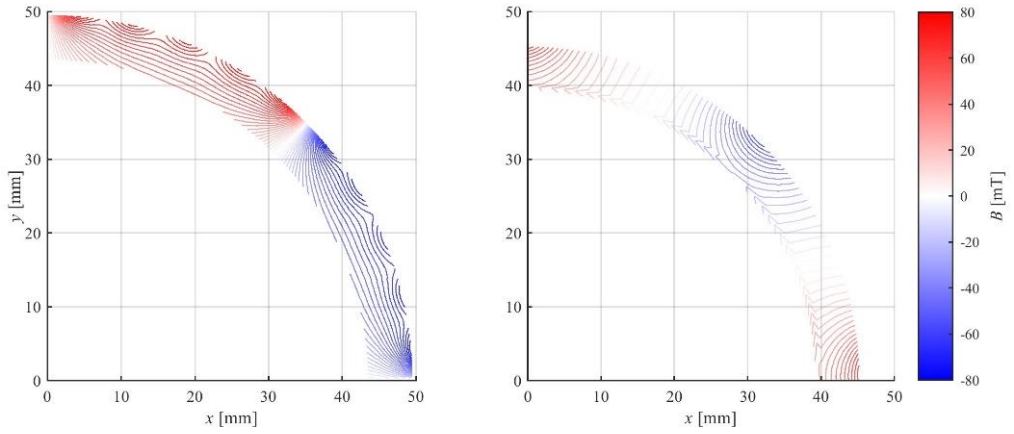

(a) (b)

This paper has been accepted for publication in the AEE journal. This is the version, which has not been fully edited and content may change prior to final publication.
Citation information: DOI 10.24425/aee.2026.158261

Fig. 8. Rotor magnetic flux density distribution at the central axial height shown as isoline plots (a) normal component (B_n), (b) tangential component (B_{tan})

For the normal component (B_n), the magnetic field varies smoothly between positive and negative values along the curved rotor path. The isolines change with radial position, becoming denser towards the outer region. Beyond a certain radius, the contours transition from smooth distributions to more localised circular patterns, indicating the presence of distinct magnetic domains. This behaviour reflects the influence of the bar magnets employed in the system, as the field structure becomes more pronounced in their vicinity, revealing localised effects determined by magnet geometry. In contrast, the tangential component (B_{tan}) exhibits a predominantly continuous dipolar pattern, with a sharper transition between positive and negative regions, indicating stronger directional variations in the field.

3.3. Harmonic analysis of rotor magnetic field components

The harmonic decomposition of the rotor magnetic field is presented for its three principal components: normal (B_n), tangential (B_{tan}), and binormal (B_b). Each component is analysed in terms of its first four dominant harmonics, providing insight into the contribution of different frequency components to the overall field distribution. Figures 9–11 present the respective components, with subplots (a–d) corresponding to the 1st, 3rd, 5th, and 7th harmonics.

The normal component (B_n) exhibits the highest amplitude among the three components, the first harmonic being the dominant contributor. The spatial distribution indicates that the fundamental harmonic defines the overall field profile, while higher-order harmonics introduce localised distortions. This observation is consistent with the findings of Wu *et al.* [31], whose analytical model showed that the dominant harmonic primarily governs the air-gap magnetic field, whereas higher-order harmonics contribute to spatial irregularities. Although the third harmonic remains significant, its amplitude is substantially lower than that of the fundamental, while the fifth and seventh harmonics contribute mainly to localised variations. The presence of these higher-order harmonics indicates field non-uniformities that may influence cogging torque.

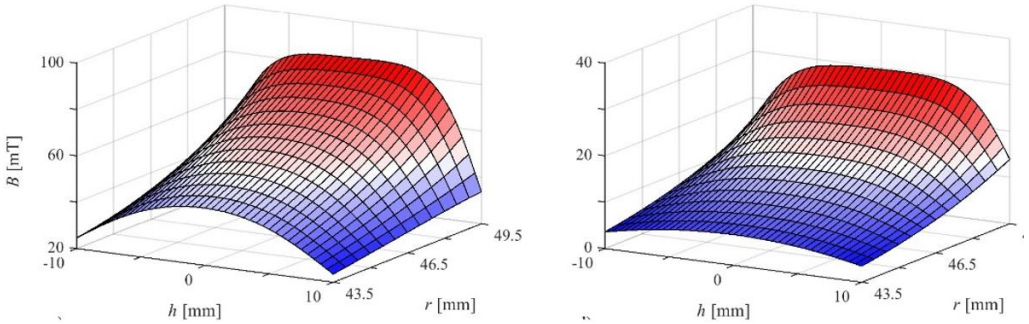

(a) (b)

This paper has been accepted for publication in the AEE journal. This is the version, which has not been fully edited and content may change prior to final publication.
Citation information: DOI 10.24425/aee.2026.158261

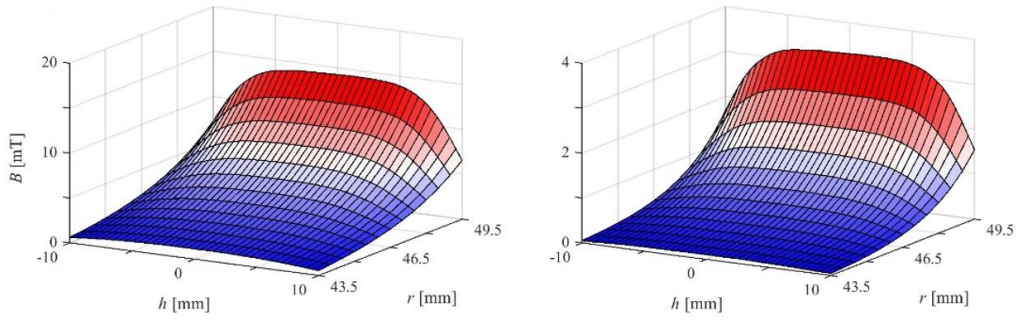

Fig. 9. Harmonic decomposition of the rotor's magnetic flux density for the normal component (B_n). Subplots (a–d) show the amplitude distribution of the 1st, 3rd, 5th, and 7th harmonics as a function of radial and axial position

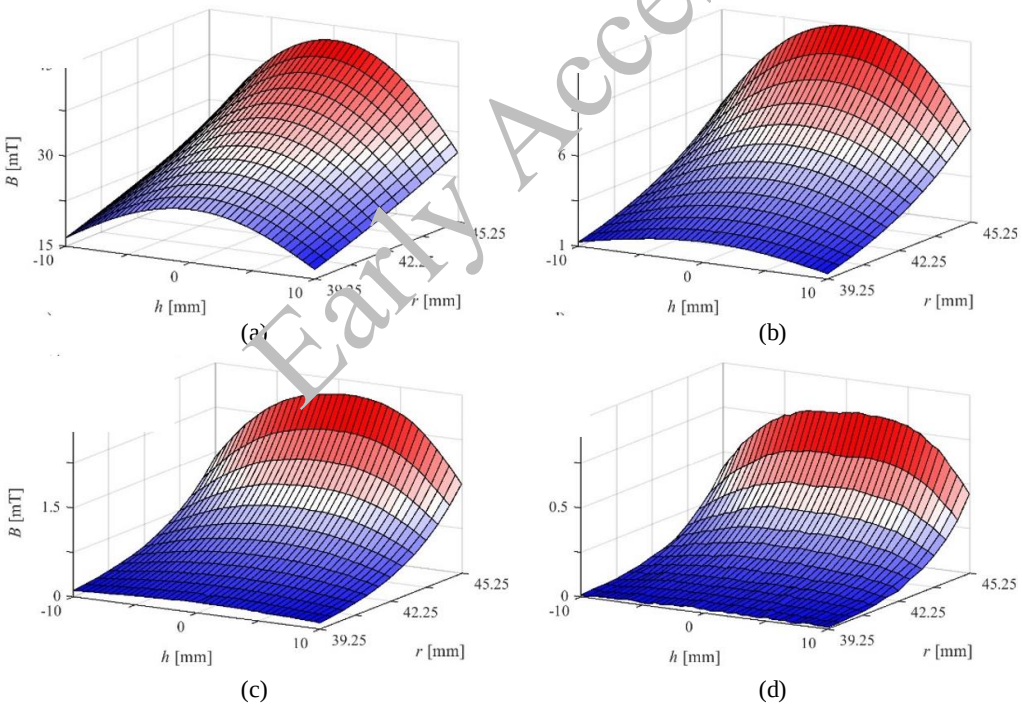

Fig. 10. Harmonic decomposition of the rotor's magnetic flux density for the tangential component (B_{tan}). Subplots (a–d) show the amplitude distribution of the 1st, 3rd, 5th, and 7th harmonics as a function of radial and axial position

The tangential magnetic field component (B_{tan}) is directly associated with torque production and reflects the interaction between the rotor and the stator. As with (B_n), the first harmonic is

This paper has been accepted for publication in the AEE journal. This is the version, which has not been fully edited and content may change prior to final publication.
Citation information: DOI 10.24425/aee.2026.158261

dominant, although with lower amplitude, and exhibits an approximately linear distribution. Higher-order harmonics (3rd, 5th, and 7th) show an exponential decrease in magnitude; however, their presence indicates potential contributions to torque ripple. These findings are consistent with those of Zhou *et al.* [32], who analysed the influence of air-gap harmonic variations on torque pulsations and demonstrated that higher-order harmonics introduce fluctuations in torque output. Similarly, Torregrossa *et al.* [33] reported that static eccentricity and partial demagnetization can amplify torque ripple effects, underscoring the importance of accurate rotor design and air-gap control.

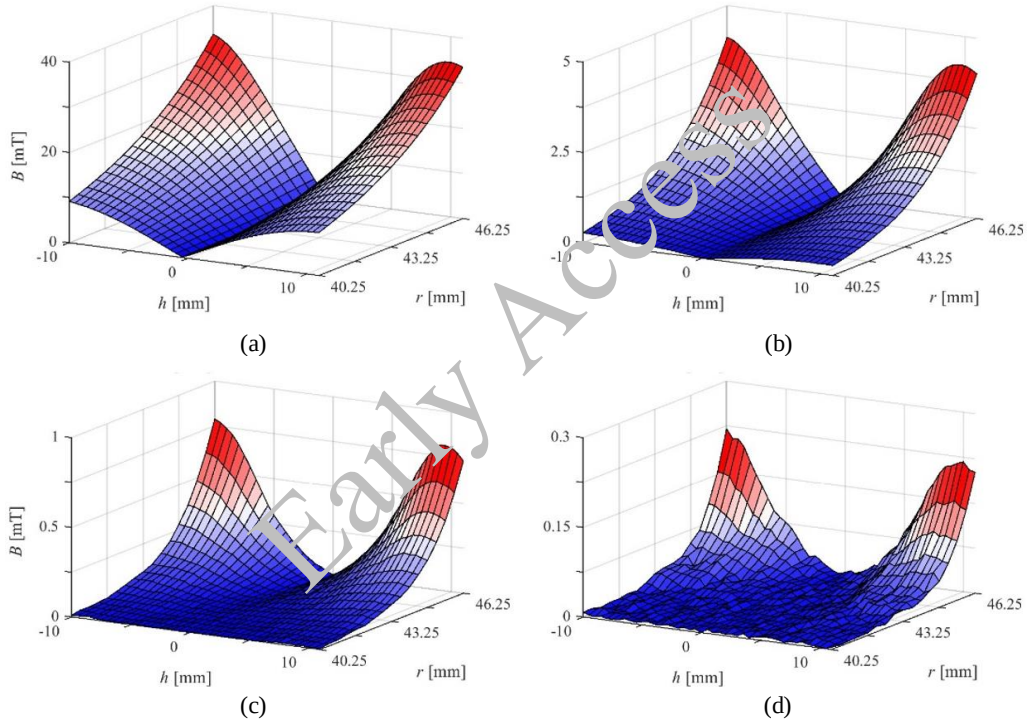

Fig. 11. Harmonic decomposition of the rotor's magnetic flux density for the tangential component (B_b). Subplots (a–d) show the amplitude distribution of the 1st, 3rd, 5th, and 7th harmonics as a function of radial and axial position

The binormal component (B_b) contributes least to the overall magnetic field but exhibits localised features that become more pronounced at higher harmonic orders. While the first harmonic remains relatively smooth, the inclusion of higher harmonics results in sharper transitions and increase oscillatory behaviour. A comparison of all three components indicates that the normal (B_n) and tangential ($B_{\tan}$) field components are of comparable magnitude and both play significant roles in machine operation. The normal component primarily influences the radial forces, whereas the tangential component is directly associated with torque generation.

This paper has been accepted for publication in the AEE journal. This is the version, which has not been fully edited and content may change prior to final publication.
Citation information: DOI 10.24425/aee.2026.158261

The binormal component (B_b) remains the weakest but demonstrates increased sensitivity to air-gap variations, particularly near the extremes.

3.4. Stator radial scan

Figure 12 presents the radial scan of the normal (B_n) and tangential (B_{tan}) magnetic field components within the stator for a coil energized with a current of 1 A. The left-hand plot illustrates the variation of B_n, while the right-hand plot shows B_{tan}. Both components are analysed as functions of angular position (θ) and the radial distance (r) from the stator pole at the central axial height.

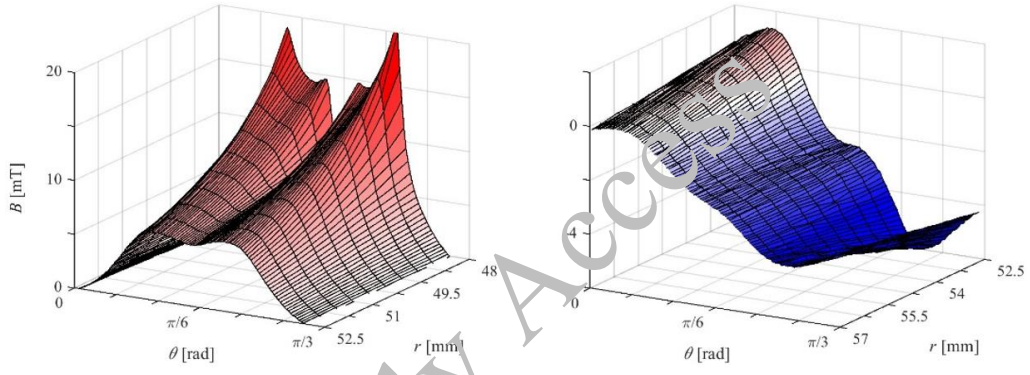

(a) (b)

Fig. 12. Stator magnetic flux density distribution at the central axial position as a function of angular and radial position: (a) normal component (B_n), (b) tangential component (B_{tan})

For the normal component (B_n), a pronounced localised field concentration is observed in the vicinity of the pole, characterised by sharp magnitude peaks. As the radial distance increases, the field intensity decreases, reflecting the decay of the normal component away from the pole structure. The field distribution also exhibits periodic angular variations consistent with the geometry and symmetry of the stator design. In particular, the observed peaks indicate a dominant contribution from the pole edges, where magnetic field intensities are highest.

In contrast, the tangential component (B_{tan}) exhibits a distinct spatial distribution. The field transitions smoothly from positive to negative values, indicating a reversal in the tangential magnetic flux across the scanned region. This behaviour suggests the presence of a circulating magnetic field around the pole, which plays a key role in torque generation and electromagnetic interactions within the machine.

The isoline plots in Fig. 13 provide further insight into the spatial distribution of the normal (B_n) and tangential (B_{tan}) magnetic field components in the stator.

This paper has been accepted for publication in the AEE journal. This is the version, which has not been fully edited and content may change prior to final publication.
Citation information: DOI 10.24425/aee.2026.158261

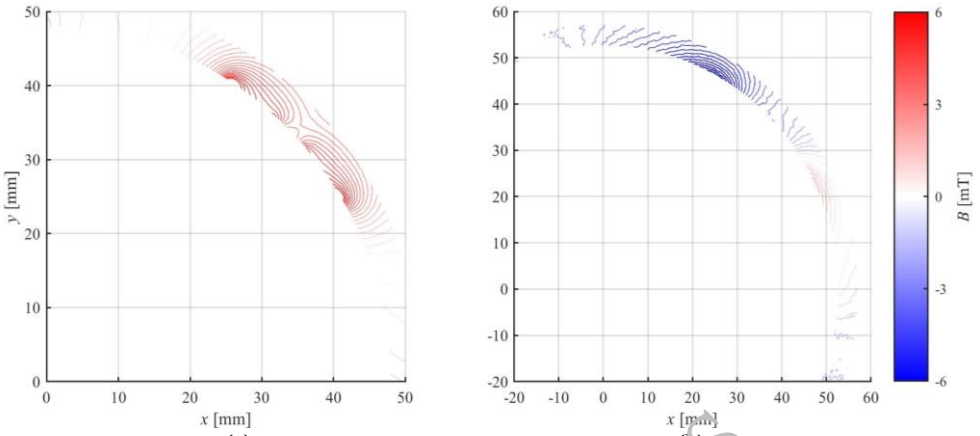

(a) (b)

Fig. 13. Stator magnetic flux density distribution at the central axial height shown as isoline plots (a) normal component (B_n), (b) tangential component ($B_{\tan}$)

In Fig. 13(a), representing the normal component (B_n), the contour lines indicate a concentration of high magnetic field values in the vicinity of the stator pole. While the field distribution appears smooth over most regions, localised circular isoline patterns suggest areas of increased field concentration, potentially associated with local magnetic saturation or pole-edge effects. As the distance from the stator pole increases, the field intensity gradually decreases, consistent with the expected radial decay of the normal component.

Figure 13(b) illustrates the tangential component ($B_{\tan}$), which exhibits a markedly different spatial pattern. The isolines show a transition from positive to negative values, confirming the rotational character of this component. This behaviour reflects a change in the direction of the tangential magnetic flux, which contributes to torque generation within the machine. Regions of denser isoline spacing indicate stronger magnetic field gradients, which may be significant for understanding the dynamic electromagnetic interactions within the stator.

4. Mathematical model of magnetic flux density distribution

4.1. Field composition and modelling scope

The magnetic flux density in the air-gap of a permanent-magnet electrical machine arises from the superposition of the magnetic field produced by the rotor magnets and the field induced by the stator currents. In the rotor reference frame, the normal and tangential components of the air-gap flux density can be expressed as

$$B_n = B_{n,\delta} + B_{n,w}, \quad B_{tan} = B_{tan,\delta} + B_{tan,w},$$

where the subscript δ denotes the contribution of the rotor magnets and w denotes the contribution of the stator windings. The present work focuses exclusively on the rotor-induced

This paper has been accepted for publication in the AEE journal. This is the version, which has not been fully edited and content may change prior to final publication.
Citation information: DOI 10.24425/aee.2026.158261

magnetic field, which defines the fundamental spatial structure of the air-gap flux density and constitutes the dominant contribution under no-load operating conditions.

4.2. Harmonic representation along the circumferential direction

Due to the geometric periodicity of multipole rotors, the rotor-induced air-gap magnetic field is periodic with respect to the circumferential coordinate θ. Consequently, both the normal and tangential components can be expanded intro truncated Fourier series as

$$B_{n,\delta}(h,r,\theta) = \sum_{k=1}^{K}[A_k(h,r)cos(k\theta) + B_k(h,r)sin(k\theta)],$$

$$B_{tan,\delta}(h,r,\theta) = \sum_{k=1}^{K}[\tilde{A}_k(h,r)cos(k\theta) + \tilde{B}_k(h,r)sin(k\theta)].$$

Here, k denotes the spatial harmonic order and $A_k(h,r), B_k(h,r)$ are the cosine and sine Fourier coefficients, respectively, defined over the axial coordinate h and the radial air-gap coordinate r. Spectral analysis of the measured data indicates that a limited number of low-order harmonics captures the majority of the magnetic energy, whereas higher-order components predominantly reflect local field distortions associated with magnet edges and segmentation boundaries.

Examination of the extracted Fourier coefficient maps reveals two key characteristics. Along the radial direction, the harmonic amplitudes exhibit a smooth, monotonic increase with increasing radius, reflecting the exponential strengthening of the magnetic field as the air-gap width decreases toward the rotor magnet surface. Along the axial direction, the variation is localised and symmetric about the magnet centre, with smooth transitions near the axial edges.

To exploit these properties, each Fourier coefficient is modelled using a separable parametric form

$$A_k(h,r) = C_k f_r(r) f_h(h), \quad B_k(h,r) = D_k f_r(r) f_h(h),$$

where $f_r(r)$ represents the radial attenuation, $f_h(h)$ is a smooth axial shaping function, C_k, D_k are harmonic scaling factors. The separability assumption significantly reduces the number of free parameters while remaining consistent with the underlying physics of magnetic field propagation in the air-gap, where radial decay and axial modulation arise from largely independent mechanisms.

4.3. Shaping functions and physical interpretation

The radial dependence of the air-gap magnetic field is primarily governed by the increasing reluctance of the magnetic circuit as the air-gap width increases. For surface-mounted permanent magnets operating below saturation, both analytical solutions and experimental observations indicate that the magnetic field decays approximately exponentially with distance from the magnet surface. Accordingly, the radial dependence of each harmonic coefficient is modelled as

$$f_r(r;\alpha) = exp\big(\alpha(r - r_0)\big),$$

This paper has been accepted for publication in the AEE journal. This is the version, which has not been fully edited and content may change prior to final publication.
Citation information: DOI 10.24425/aee.2026.158261

where r_0 denotes the reference radial position closest to the magnet surface, and $\alpha > 0$ is the radial attenuation coefficient.

The parameter α quantifies the effective magnetic decay rate in the air-gap and implicitly incorporates the influence of magnet strength, air-gap permeability, and leakage flux. Unlike polynomial or rational approximations, the exponential form guarantees monotonic decay, bounded behaviour, and physical consistency over the entire radial domain.

The axial dependence of the air-gap magnetic field reflects the finite length of the permanent magnets and the associated fringing effects at their axial edges. Experimental field distribution consistently shows that the axial variation of the magnetic field is smooth, symmetric with respect to the magnet centre, and strongly localised within the magnet span. To capture these characteristics while maintaining a compact analytical representation, three alternative axial shaping functions were considered in this study.

The first axial model is a smoothed top-hat profile defined using the difference of two error functions.

$$f_h(h; h_0, L, \delta) = \frac{1}{2}\left[erf\left(\frac{h-h_0+L/2}{\delta}\right) - erf\left(\frac{h-h_0-L/2}{\delta}\right)\right].$$

This formulation represents an idealized magnet of finite axial length L, centered at h_0, with a smooth transition of width δ at the magnet edges. From a physical perspective, this model corresponds to a uniformly magnetized block whose abrupt axial boundaries are softened by magnetic fringing and finite permeability effects. The error-function smoothing avoids discontinuities in the field and ensures differentiability, which is essential for gradient-based optimization and force calculations.

The second axial model employs a super-Gaussian function

$$f_h(h; h_0, \sigma, n) = exp\left(-\left|\frac{h-h_0}{\sigma}\right|^n\right).$$

This formulation generalizes the classical Gaussian profile by introducing an exponent n, which controls the sharpness of the axial confinement. For $n = 2$, the model reduces to a standard Gaussian distribution, while larger values of n yield increasingly flat central regions with steeper edge decay. Physically, the super-Gaussian model captures the combined effect of distributed magnetization, axial leakage, and fringing flux in a flexible yet smooth manner. The parameter σ represents the effective axial extent of the magnetic field, while n governs how rapidly the field diminishes near the magnet boundaries.

The third axial model is a symmetric double-exponential function

$$f_h(h; h_0, \lambda) = exp\left(-\frac{|h-h_0|}{\lambda}\right).$$

This model assumes that the magnetic field decays exponentially away from the magnet centre along the axial direction. The decay length λ directly represents the characteristic distance over which axial fringing effects dominate. From a physical standpoint, the double-exponential model reflects situations where no well-defined plateau exists in the central region. Its simplicity

This paper has been accepted for publication in the AEE journal. This is the version, which has not been fully edited and content may change prior to final publication.
Citation information: DOI 10.24425/aee.2026.158261

and minimal parameter count make it attractive for reduced-order modelling and rapid evaluation, albeit at the cost of reduced flexibility compared to the other two models.

4.4. Optimization and parameter identification procedure

The identification of the parametric model is performed independently for each harmonic order and for each Fourier coefficient (A_k,B_k). For a given harmonic, the following steps are applied:

1. Initial separability extraction,
2. A singular value decomposition (SVD) of the measured coefficient map is used to obtain an initial estimate of the dominant radial and axial profiles. This provides robust initial guesses for the nonlinear parameters,
3. Nonlinear least-squares fitting,
4. The full parametric model is fitted using constrained nonlinear least squares, minimizing the Frobenius norm of the residual between measured and modelled coefficient maps,
5. Independent optimization of cosine and sine coefficients,
6. The $A_k(h,r)$ and $B_k(h,r)$ coefficients are optimized separately, allowing the model to capture asymmetries and phase shifts that cannot be represented by magnitude-only formulations.

All optimizations are carried out using a trust-region reflective algorithm, with convergence achieved when further parameter updates no longer reduce the normalized residual error.

4.5. Model validation

To assess the influence of the axial shaping function on modelling accuracy, three alternative axial profiles were investigated: a smoothed top-hat function based on the error function, a super-Gaussian profile, and a double-exponential function. Each formulation was applied within the same separable parametric framework and identified using an identical optimization procedure, ensuring a fair and consistent comparison. The resulting models were evaluated separately for the normal and tangential components of the air-gap magnetic flux density.

Table 2 summarizes the global error metrics obtained for each axial model, expressed in terms of the root-mean-square error and the normalized root-mean-square error, both computed over the full spatial domain and accumulated over one complete electrical rotation. These scalar indicators provide an initial quantitative comparison of the three axial shaping strategies and highlight their relative ability to reproduce the measured harmonic field amplitudes. While the table captures the overall modelling performance, a more detailed understanding of the error mechanisms requires examination of the spatial distribution of the residuals, which is addressed in the following section.

For the normal component B_n, which dominates the magnetic energy in the air-gap and is most sensitive to axial field confinement, the super-Gaussian axial model achieves the lowest error levels, with an RMSE of 3.56 and an RMSN of 4.46%. The smoothed top-hat model yields very similar accuracy (RMSE = 3.59, RMSN = 4.50%), indicating that both formulations capture the main axial field structure effectively. In contrast, the double-exponential model

This paper has been accepted for publication in the AEE journal. This is the version, which has not been fully edited and content may change prior to final publication.
Citation information: DOI 10.24425/aee.2026.158261

exhibits higher errors (RMSE = 4.95, RMSN = 6.19%), reflecting its limited ability to represent a quasi-uniform magnetic field in the central magnet region and its overly rapid decay away from the axial centre. For the tangential component $B_{\tan}$, all three models demonstrate comparable performance, with RMSN values below 4%. The super-Gaussian and smoothed top-hat models provide nearly identical accuracy, while the double-exponential model shows only a marginal increase in error.

Table 2. Global modelling accuracy for the normal (B_n) and tangential ($B_{\tan}$) components of the air-gap magnetic flux density obtained using the three proposed axial shaping functions. The root-mean-square error and normalized root-mean-square error are computed over the full (r, h) domain and accumulated over one complete electrical rotation

Axial model	Component	RMSE	RMSN (%)
Smoothed top-hat (erf)	B_n	3.59	4.50
	$B_{\tan}$	2.31	3.76
Super-Gaussian	B_n	3.56	4.46
	$B_{\tan}$	2.3[illegible]	3.75
Double-exponential	B_n	4.95	6.19
	$B_{\tan}$	2.43	3.95

Figure 14 presents the spatial distribution of the normalized root-mean-square error of the reconstructed air-gap magnetic field, evaluated over one complete electrical rotation and mapped as a function of the axial coordinate h and the air-gap radius r. The two subfigures correspond to the normal (B_n) and tangential ($B_{\tan}$) components and are evaluated over their respective radial domains.

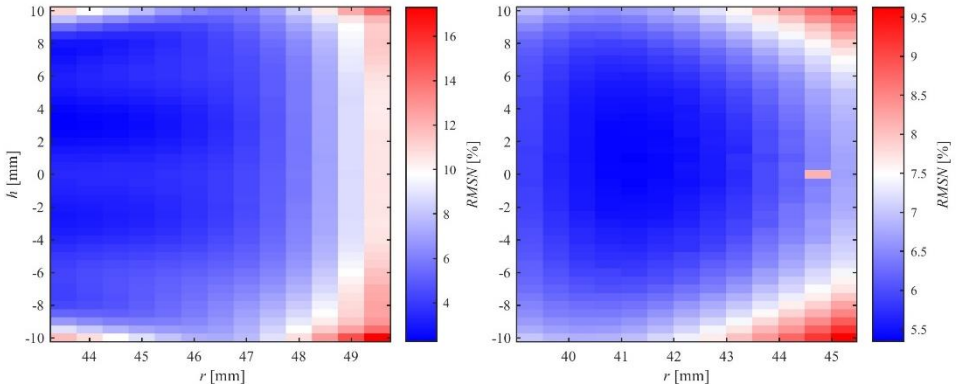

(a) (b)

This paper has been accepted for publication in the AEE journal. This is the version, which has not been fully edited and content may change prior to final publication.
Citation information: DOI 10.24425/aee.2026.158261

Fig. 14. Spatial distribution of the modelling error expressed as RMSN: (a) normal component B_n; (b) tangential component $B_{\tan}$

For the normal component B_n, the RMSN values remain relatively low and uniform over a large portion of the (*h*, *r*) domain. In the central axial region, approximately between ± 8 mm, the RMSN remains consistently below 5% across most of the radial range. This indicates that, away from the axial boundaries, the magnetic field distribution is well captured by the proposed separable parametric model and that the assumed axial shaping function accurately represents the dominant field variation.

Along the radial direction, a clear trend is observed for B_n. At smaller radii, corresponding to locations farther from the magnet surface, the RMSN remains low and exhibits only weak dependence on r. As the radius increases and the evaluation points approach the magnet surface, the RMSN gradually increases, particularly near the axial extremities. This behaviour reflects the increasing complexity of the magnetic field in the vicinity of the magnets, where flux density gradients become stronger and axial-radial coupling effects become more pronounced.

The highest RMSN values for B_n, reaching approximately 16%, are localised in regions combining large radius and large absolute axial coordinate, that is, near the magnet corners. These regions are dominated by fringing flux and local field spreading, which introduce three-dimensional field components not explicitly represented in the separable analytical formulation. Importantly, the increase in RMSN is smooth and continuous, without abrupt transitions or isolated peaks, indicating that the modelling error arises from systematic physical effects rather than from numerical instability or parameter misidentification.

The RMSN map for the tangential component $B_{\tan}$ exhibits a similar smooth and well-behaved distribution over the evaluated (*h*, *r*) domain, with RMSN values remaining below approximately 4% across most of the axial extent. At comparable radial positions, the error levels are similar to those observed for the normal component. As the radius increases toward the maximum evaluated value, a gradual increase in RMSN becomes evident, particularly near the axial extremities, indicating reduced model accuracy close to the magnet edges.

Residual deviations near the magnet boundaries can be attributed to unmodeled effects such as edge saturation and local variations in magnetisation. Despite these limitations, the error levels remain within acceptable bounds for analytical torque and back-EMF estimation, confirming that the model generalises well beyond the identification dataset. The primary strength of the proposed formulation lies in its compact analytical structure, which maintains clear physical interpretability while remaining computationally efficient for system-level electromagnetic simulations. Its principal limitation is the assumption of smooth, periodic axial variation, which may slightly underestimate local distortions in highly segmented or skewed rotors. Nevertheless, the achieved accuracy and spatial consistency establish the model as a robust foundation for further Multiphysics coupling and dynamic performance analyses.

This paper has been accepted for publication in the AEE journal. This is the version, which has not been fully edited and content may change prior to final publication.
Citation information: DOI 10.24425/aee.2026.158261

5. Summary

This study represents a transition from simulation-driven analysis to experimental validation using a robotic magnetic field scanning system. While the results confirm established motor theory - namely the exponential radial decay and axial attenuation of the normal field, as well as the dipolar nature of the tangential component - they also reveal finer spatial features that are often neglected in numerical simulations. Higher-order harmonics and localised distortions in the binormal component are identified, highlighting their potential influence on electromagnetic noise, vibration, and stability under non-ideal conditions such as eccentricity or rotor wobbling.

These findings emphasise the need to refine analytical motor models for scenarios involving asymmetric flux distributions arising from rotor skew, eccentricity, or manufacturing tolerances. Harmonic analysis further demonstrates that higher-order components, although frequently neglected, can contribute significantly to torque ripple and transient behaviour, especially in precision or low-noise applications.

The proposed robotic scanning system effectively bridges the gap between numerical modelling and experimental validation by enabling high-resolution, multidimensional magnetic field measurements. The acquired data support improved rotor geometry optimisation and facilitate the development of advanced algorithms for rotor position estimation and control. Nevertheless, certain experimental limitations remain. Accurate sensor alignment with respect to the robotic tool centre point requires precise coordinate transformations, and minor misalignments or post-processing errors may introduce uncertainty. In addition, mechanical vibrations and thermal variations in the test rig can affect measurement repeatability, particularly during high-resolution scans.

Beyond these experimental considerations, the validated analytical model provides a compact and physically interpretable framework for reconstructing rotor magnetic fields with high spatial and harmonic fidelity. The sequential parametric optimisation strategy proved essential for numerical stability, reducing parameter coupling and improving convergence compared with a global fitting approach. As a result, a mean reconstruction error below 6% was achieved across the air-gap domain, with the exponential - sinusoidal formulation accurately capturing both dominant field decay and secondary oscillatory effects related to magnet geometry and leakage paths.

Residual discrepancies are primarily confined to magnet edges and regions of strong fringing, where assumptions of smooth axial periodicity and uniform magnetisation become less valid. Despite this, the achieved accuracy demonstrates that the proposed analytical formulation can replace finite-element analysis in many steady-state evaluations, while remaining computationally efficient and closely linked to measurable physical quantities. This makes it particularly suitable for rapid torque, force, and back-EMF estimation in iterative design and embedded control applications.

Future work will focus on controlled experimental investigations incorporating known geometric deviations - such as eccentricity, skew, or wobbling - to quantify their effects on flux distribution, harmonic distortion, and torque ripple. Coupling experimentally derived field maps

This paper has been accepted for publication in the AEE journal. This is the version, which has not been fully edited and content may change prior to final publication.
Citation information: DOI 10.24425/aee.2026.158261

with advanced control and estimation algorithms offers a pathway towards condition-aware motor drives capable of compensating for manufacturing tolerances and dynamic imbalances in real time. Extending the robotic scanning approach to dynamic and temperature-dependent measurements will further enhance its applicability to co-design, diagnostics, and fault-tolerant machine operation.

References.

[1] Niu L., Zhang M., *Rotor topology optimization and electromagnetic performance analysis of interior permanent magnet synchronous motors for electric vehicle applications*, The Journal of Engineering, vol. 2023, no. 2, e212240 (2023), DOI: 10.1049/tje2.12240.
[2] Nishanth F., Khamitov A., Severson E.L., *Design of electric machine windings to independently control multiple airgap harmonics*, IEEE Transactions on Industry Applications, vol. 60, no. 2, pp. 3039–3050 (2024), DOI: 10.1109/tia.2023.3331662.
[3] Mbadiwe E.I., Bin Sulaiman E., *Design and optimization of outer-rotor permanent magnet flux switching motor using transverse segmental rotor shape for automotive applications*, Ain Shams Engineering Journal, vol. 12, no. 1, pp. 507–516 (2021), DOI: 10.1016/j.asej.2020.08.007.
[4] Bai K., Lee K.-M., *A sensor-less motion sensing method of a 3-dof permanent magnet spherical motor*, IFAC Proceedings Volumes, vol. 46, no. 5, pp. 160–164 (2013), DOI: 10.3182/20130410-3-CN-2034.00121.
[5] Bai K., Lee K.-M., *Direct field-feedback control of a ball-joint-like permanent-magnet spherical motor*, IEEE/ASME Transactions on Mechatronics, vol. 19, no. 3, pp. 975–986 (2014), DOI: 10.1109/TMECH.2013.2264565.
[6] Akrami M., Jamshidpour E., Frick V., *Application of Hall position sensor in control and position estimation of PMSM: a review*, 2023 IEEE International Conference on Environment and Electrical Engineering and 2023 IEEE Industrial and Commercial Power Systems Europe (EEEIC/ICPS Europe), pp. 1–6 (2023), DOI: 10.1109/EEEIC/ICPSEurope57605.2023.10194763.
[7] Qu K., Pang P., Hua W., *High-precision rotor position fitting method of permanent magnet synchronous machine based on Hall-effect sensors*, Energies, vol. 17, no. 22 (2024), DOI: 10.3390/en17225625.
[8] Mirzaeva G., Saad K.I., *Advanced diagnosis of stator turn-to-turn faults and static eccentricity in induction motors based on internal flux measurement*, IEEE Transactions on Industry Applications, vol. 54, no. 4, pp. 3961–3970 (2018), DOI: 10.1109/TIA.2018.2821098.
[9] Baszyński M., *Low cost, high accuracy real-time simulation used for rapid prototyping and testing control algorithms on example of BLDC motor*, Archives of Electrical Engineering, vol. 65, no. 3, pp. 463–479 (2016), DOI: 10.1515/aee-2016-0034.
[10] Min'an Tang, Chenyu Wang, Yianhang Luo, *Predictive current control for permanent magnet synchronous motor based on internal model control observer*, Archives of Electrical Engineering, vol. 71, no. 2, pp. 343–362 (2022), DOI: 10.24425/aee.2022.140715.
[11] Li Ming, Lun Shuxian, Mu Haiqi, Wang Wei, *A novel temperature calculation method of canned permanent magnet synchronous motor for vacuum pump*, Archives of Electrical Engineering, vol. 73, no 1, pp. 87–104 (2024), DOI: 10.24425/aee.2024.148859.
[12] Zhang L., Zheng G., Li Y., Li X., Sun X., Ma J., Zou M., Wang D., Zhang S., Li Y., Liu S., Sun W., *An economical three-dimension (3-D) Hall device on 0.15-μm bipolar-CMOS-DMOS (BCD) platform*, IEEE Sensors Journal, vol. 24, no. 7, pp. 9828–9834 (2024), DOI: 10.1109/JSEN.2024.3368045.
[13] Gordon D., Lundsten R., Chiarodo R., Helms H., *A fluxgate sensor of high stability for low field magnetometry*, IEEE Transactions on Magnetics, vol. 4, no. 3, pp. 397–401 (1968), DOI: 10.1109/TMAG.1968.1066332.

This paper has been accepted for publication in the AEE journal. This is the version, which has not been fully edited and content may change prior to final publication.
Citation information: DOI 10.24425/aee.2026.158261

[14] Oelsner G., Ijsselsteijn R., Scholtes T., Kruger A., Schultze V., Seyffert G., Werner G., Jager M., Chwala A., Stolz R., *Integrated optically pumped magnetometer for measurements within Earth's magnetic field*, Phys. Rev. Appl., vol. 17, 024034 (2022), DOI: 10.1103/PhysRevApplied.17.024034.
[15] Vervaeke K., *Large area magnetic field camera for inline motor magnet inspection*, 2012 2nd International Electric Drives Production Conference (EDPC), pp. 1–9 (2012), DOI: 10.1109/EDPC.2012.6425114.
[16] Vervaeke K., *3-axis magnetic field camera for ultrafast and high resolution inspection of permanent magnets*, 2014 4th International Electric Drives Production Conference (EDPC), pp. 1–5 (2014), DOI: 10.1109/EDPC.2014.6984397.
[17] Vervaeke K., *6D magnetic field distribution measurements of permanent magnets with magnetic field camera scanner*, 2015 5th International Electric Drives Production Conference (EDPC), pp. 1–4 (2015), DOI: 10.1109/EDPC.2015.7323203.
[18] Feng J., Zhang X., Lu S., Yang F., *A single-stage enhancement-identification framework for pipeline MFL inspection*, IEEE Transactions on Instrumentation and Measurement, vol. 71, pp. 1–13 (2022), DOI: 10.1109/TIM.2022.3176285.
[19] Shaw G., Kramer R.B.G., Dempsey N.M., Hasselbach K., *A scanning Hall probe microscope for high resolution, large area, variable height magnetic field imaging*, Review of Scientific Instruments, vol. 87, no. 11, 113702 (2016), DOI: 10.1063/1.4967255.
[20] Nasir M., Shoaib M., Hassan M.U., Anwar M.S., *Design and implementation of a versatile magnetic field mapper for 3D volumes*, HardwareX, vol. 12, e00356 (2022), DOI: 10.1016/j.ohx.2022.e00356.
[21] Pilat A.K., *Robotized magnetic field test*, Measurement Automation Robotics (in Polish), vol. 13, no. 157, pp. 18–21 (2009).
[22] Ahmed H., Mohsin A., Hong S.-C., Lee J.-R., Ihn J.-B., *Robotic laser sensing and laser mirror excitation for pulse-echo scanning inspection of fixed composite structures with non-planar geometries*, Measurement, vol. 176, 109109 (2021), DOI: 10.1016/j.measurement.2021.109109.
[23] Cao L., Russo D., Felton K., Salley D., Sharma A., Keenan G., Mauer W., Gao H., Cronin L., Lapkin A.A., *Optimization of formulations using robotic experiments driven by machine learning DOE*, Cell Reports Physical Science, vol. 2, no. 1, 100295 (2021), DOI: 10.1016/j.xcrp.2020.100295.
[24] Wenninger J., Silber S., Weisengruber P., *Machine-made coil winding with a collaborative industrial robot* (2021).
[25] Milanowski H., Pilat A.K., *Towards experimental insight into magnetic flux distribution within the air gap of permanent magnet synchronous drive*, 2024 28th International Conference on Methods and Models in Automation and Robotics (MMAR), pp. 334–339 (2024), DOI: 10.1109/MMAR62187.2024.10680794.
[26] Milanowski H., Pilat A., *Supplementary material for bringing automation to electromagnetic: Robotic scanning of magnetic field in electric drives* (2025), DOI: 10.5281/zenodo.15538622.
[27] Pilat A.K., *6 pole AMB as a drive of elliptic rotor - initial study supported by the virtual prototype*, International Journal of Applied Electromagnetics and Mechanics, vol. 63, no. 1, 153 (2020), DOI: 10.3233/JAE-209006.
[28] Milanowski H., Pilat A.K., *Comparison of identified and Simscape model of human leg motion*, 2020 International Conference Mechatronic Systems and Materials (MSM) (2020), DOI: 10.1109/MSM49833.2020.9201736.
[29] Cheng W., Sun Y., Yu L., Huang L., Lv Y., Li L., *Analytical solution to magnetic field distribution of a parallel magnetised rotor with cylindrical or ring-type permanent magnet*, IET Electric Power Applications, vol. 9, no. 6, pp. 429–437 (2015), DOI: 10.1049/iet-epa.2014.0162.
[30] Li Z., Wan Y., Xia Y., Gong F., Wang Q., Chen F., *Analysis of electromagnetic characteristic in the interior permanent magnet brushless DC motor*, Mathematical Models in Engineering, vol. 8, no. 3, pp. 91–97 (2022), DOI: 10.21595/mme.2022.22950.
[31] Wu Z., Zuo S., Hu S., Hu X., *Analytical modelling of air-gap magnetic field of interior permanent magnet synchronous motors*, IET Electric Power Applications, vol. 14, no. 11, pp. 2101–2110 (2020), DOI: 10.1049/iet-epa.2019.0948.

This paper has been accepted for publication in the AEE journal. This is the version, which has not been fully edited and content may change prior to final publication.
Citation information: DOI 10.24425/aee.2026.158261

[32] Ma C., Zhou S., Yang N., Degano M., Gerada C., Fang J., Liu Q., *Characteristic analysis and direct measurement for air gap magnetic field of external rotor permanent magnet synchronous motors in electric vehicles*, IET Electric Power Applications, vol. 14, no. 10, pp. 1784–1794 (2020), DOI: 10.1049/iet-epa.2019.0931.

[33] Torregrossa D., Khoobroo A., Fahimi B., *Prediction of acoustic noise and torque pulsation in PM synchronous machines with static eccentricity and partial demagnetization using field reconstruction method*, IEEE Transactions on Industrial Electronics, vol. 59, no. 2, pp. 934–944 (2012), DOI: 10.1109/TIE.2011.2151810.